Journal of Mathematical Research with Applications
Mar., 2024, Vol. 44, No. 2, pp. 269–284
DOI:10.3770/j.issn:2095-2651.2024.02.012
Http://jmre.dlut.edu.cn

Linear and Nonlinear Solutions of Interfacial Waves Due to a Doublet

Di LIU[1], **Zhen WANG**[2,*]

1. *School of Mathematics, Jilin University, Jilin* 130012, *P. R. China;*
2. *School of Mathematical Sciences, Beihang University, Beijing* 100191, *P. R. China*

Abstract Steady two-dimensional potential flows of two-layer fluids with a submerged doublet in the lower layer are considered. Both linear analytical solutions and fully nonlinear solutions based on boundary integral equation methods are obtained. Nonlinearity strongly influences the downstream wave height and leads to a slight phase difference. When the Froude number is small, wave height fast gets its maximum as the Froude number increases. While wave-less solutions may be obtained if the Froude number is very large. Afterward, the interfacial waves due to one point vortex or a vortex pair are compared with those due to a doublet. It is found that the nonlinear wave profiles due to a doublet are quite close to those due to a vertical vortex pair if the distance between the vortex pair is set appropriately.

Keywords interfacial waves; doublet; boundary integral equation method; linear solutions

MR(2020) Subject Classification 76B55; 76M45; 76M15; 65R20

1. Introduction

Internal gravity waves, which are wave motions under the surface, are ubiquitous in oceans. Stratification of fluids generates due to the differences of the salty and temperature of seawaters, and large internal waves can be created even by small disturbances. For example, an extreme internal wave with an amplitude of 240m and a current velocity of 2.55 m/s was reported in the northern South China Sea [1]. Along with the exploration of oceans, the influences of internal waves on marine obstructures [2, 3], the mechanisms of generations of internal waves, and their characters of evaluations are gradually attracting the attention of researchers [4]. In particular, as a place rich in oil and other resources, there are also frequent occurrences of internal waves in the South China Sea. Therefore, it is necessary to understand the mechanisms of generations, transportation, and evaluations of the internal waves to ensure the safety of offshore operations [5, 6].

One can recall that flows around the moving object(s) associated with the free surface is a classical topic in hydrodynamics due to its relationships with the practical applications, e.g., wave making resistance of ships. Under the assumption of ideal irrotational fluids, the problem

Received February 20, 2023; Accepted January 6, 2024
Supported by the National Natural Science Foundation of China (Grant Nos. 52171251; U2106225).
* Corresponding author
E-mail address: diliu20@mails.jlu.edu.cn (Di LIU); wangzhen@dlut.edu.cn (Zhen WANG)

of steady flows due to a mathematical singularity submerged in fluids represents simple aspect of the above problems, so it has been studied by many researchers of different communities. Traditionally, under the assumption that the strength of the singularity is small, the velocity potential and the surface deformation are obtained via the linearization and integral transform techniques. Wehausen and Laitone [7] reviewed the solutions for source, vortex and dipole in a fluid of finite and infinite depth. Results for more complicated situations can be referred to [8] in details. Furthermore, by virtue of the development of the computer, nonlinear free-surface problems are considered and the effects of nonlinearity depict different characteristics. For instance, works of Forbes point out that linearized theory may under-estimate the drag force of waves and even worse, gives very different results compared with nonlinear methods. This suggests that nonliearity of flow problems should be examined in details.

It may be natural to extend from flows of a single fluids to those of two fluids or more complex stratified fluids. Many works focus on the two-layer fluids of finite depth, or the case when the lower fluid is of infinite/finite constant depth and the upper being of infinite height. Gorgui and Kassem [9] derived velocity potentials describing different types of singularities in one of the two fluids in the latter case. The method they used is an extension of that used in the case of one fluid. Yeung, Nguyen [10] and Wei, Lu, Dai [11] applied the Green's function method to study the two-layer flows problems associated with linearized boundary conditions due to a moving source and a dipole (a source-sink pair), respectively. Velocity potentials of two layers and wave patterns of both internal and surface waves are obtained. However, if the density difference between two fluids is quite small, the effect of the free surface may be neglected. Under the assumptions of lid-rigid, Wang et al. [12] studied the interracial waves due to a point vortex in the case when the lower layer is of infinite depth and the height of the upper layer is constant. Both linearized and fully nonlinear solutions based on boundary integral methods are obtained, and obviously nonlinear effects were observed. Especially, when the strength of one negative vortex is large enough, the wave-less solutions are obtained only for nonlinear results. In this works we extend these results to the interracial waves due to one doublet singularity, and both linearized and nonlinear solutions are obtained. In potential flow theory, the doublet can be used to model steady flows around a cylinder in infinite fluids. In practice, it can also simulate other flows, such as the famous Kelvin ship waves [13, 14]. Next, to further learn about the characteristics of flows of different types of singularities, qualitative comparisons of nonlinear/linearized solutions between vortices and doublets are implemented. Especially, for the configuration of a vertical counter-rotating vortex pair, if the distance of the vortex pair is chosen intentionally , only downstream waves for a doublet can coincide with those for a vertical vortex pair due to a doublet. However, it is easy to think about if recalling the fact that a doublet can be seen as the limit of a vertical equal-strength counter-rotating vortex pair.

This paper is organized as follows: In Section 2, the model of two-layer flows is established and the corresponding boundary integral equations are obtained. In Sections 3 and 4, both the linear solutions and the nonlinear numerical solutions are obtained. In Section 5, we examine the interfacial wave profiles for different parameters. Comparisons of the effects of a doublet and

a point vortex are also provided. The conclusion is given in Section 6.

2. Modelling

The configuration of this model is similar to that in many works of two-dimensional two-layer potential flows. A Cartesian coordinate system is established, in which the x-axis is located along with the undisturbed interface, and the y-axis points vertically. A doublet of strength M submerged in the lower layer is located on the y axis, and the distance between it and the undisturbed interface is H. In the following works, the subscripts 1 and 2 correspond to the physical quantities of the upper and lower layers, respectively. The depth of the upper layer is T, while the low layer is of infinite depth. The densities of these two layers are ρ_1, ρ_2, and the upstream uniform velocities are c_1, c_2. Choosing the length scale H and the time scale H/c_2, we reformulate the problem into the dimensionless model, and the following dimensionless parameters are introduced:

$$F=\frac{c_2}{\sqrt{gH}},\ m=\frac{M}{c_2H^2},\ \rho=\frac{\rho_1}{\rho_2},\ c=\frac{c_1}{c_2},\ \alpha=\frac{T}{H},$$

where F is the Froude number, m is the dimensionless strength of the doublet, ρ is the density ratio of two layers of fluids, c is the ratio of the far upstream uniform velocities, and α is the dimensionless depth of the upper layer. This dimensionless model can be seen as the two-layer flows past a cylinder of radius $\sqrt{m/2\pi}$. Here we set $c=1$ to avoid the potential Kelvin-Helmholtz instability, and $0<\rho<1$ to ensure the stability of the two-layer system. Figure 1 demonstrates this dimensionless model. $y=\eta(x)$ describes the interfacial wave profiles, and $z^*=-\mathrm{i}$ is the location of the doublet in the lower layer.

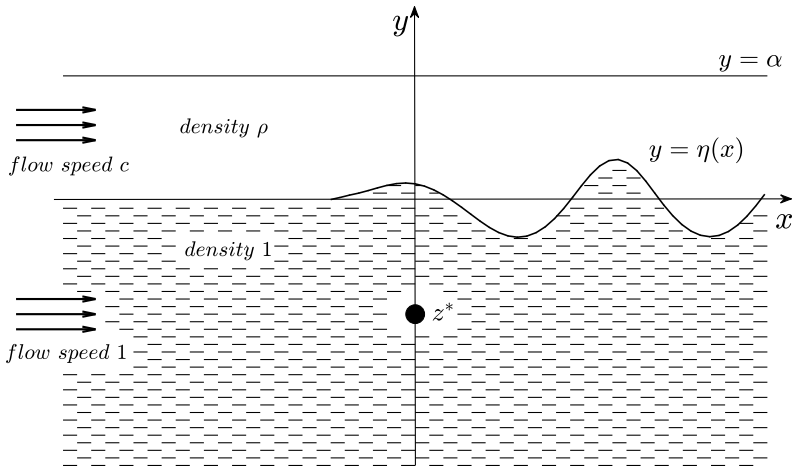

Figure 1 The schematic diagram of interfacial waves due to one submerged doublet in the lower layer

Since we focus on the two-dimensional potential flows, potential functions ϕ_1,ϕ_2, stream functions ψ_1,ψ_2 are introduced and they satisfy the Cauchy-Riemann equations

$$\frac{\partial\phi_j}{\partial x}=\frac{\partial\psi_j}{\partial y},\ \frac{\partial\phi_j}{\partial y}=-\frac{\partial\psi_j}{\partial x},\quad j=1,2. \tag{2.1}$$

Thus, two complex potentials

$$f_j(z) = \phi_j(x, y) + \mathrm{i}\psi_j(x, y), \quad j = 1, 2,$$

which are analytical functions, are introduced for two layers to formulate the problem into the form of boundary integral equations. In the neighborhood of $z^* = -\mathrm{i}$, where the doublet locates, f_2 satisfies

$$f_2 \to z - z^* + \frac{m}{2\pi}\frac{1}{z - z^*}, \quad \text{as } z \to z^*. \tag{2.2}$$

The upstream radiation conditions for two-layer fluids and the interface are

$$f_1 \to cz, \ f_2 \to z, \ \eta \to 0, \ \mathrm{Re}[z] \to -\infty; \ f_2 \to z, \ \mathrm{Im}[z] \to -\infty, \tag{2.3}$$

where $\mathrm{Re}[\cdot]$, $\mathrm{Im}[\cdot]$ means taking the real and imaginary part, respectively. Next, the upper surface of the upper layer is set to be a rigid lid. Both the upper surface of the upper layer and the interface satisfy the unpenetrable conditions

$$\frac{\partial \phi_1}{\partial y} = 0, \quad \text{on} \quad y = \alpha \tag{2.4}$$

and

$$\frac{\partial \phi_j}{\partial y} = \frac{\partial \phi_j}{\partial x}\frac{\mathrm{d}\eta}{\mathrm{d}x}, \quad j = 1, 2, \quad \text{on} \quad y = \eta(x). \tag{2.5}$$

Following the approach of [12, 15–17], here we use the arclength parameter s to parametrize the fluid interface:

$$(x, \eta(x)) = (x(s), y(s)).$$

Naturally, the arclength condition

$$\Big(\frac{\mathrm{d}x}{\mathrm{d}s}\Big)^2 + \Big(\frac{\mathrm{d}y}{\mathrm{d}s}\Big)^2 = 1 \tag{2.6}$$

must be satisfied. Besides, the Bernoulli's equation

$$\rho\Big(\frac{\mathrm{d}\phi_1}{\mathrm{d}s}\Big)^2 - \Big(\frac{\mathrm{d}\phi_2}{\mathrm{d}s}\Big)^2 + \frac{2(\rho - 1)y}{F^2} = \rho c^2 - 1 \tag{2.7}$$

is obtained on the interface from the equality of the pressure on the interface. One can see [12] for the detailed process of derivation.

Introducing an analytical function

$$G_1(z) = \frac{\mathrm{d}f_1}{\mathrm{d}z} - c$$

for the upper layer, and applying the Cauchy integral formula, we have

$$\oint_{\Gamma_1} \frac{G_1(\xi)}{\xi - z}\,\mathrm{d}\xi = \pi\mathrm{i}G_1(z), \tag{2.8}$$

where $z = z(s)$ is an arbitrary fixed point on the interface. The integral path Γ_1 consists of the interface $y = \eta(x)$ excluding the fixed point $z = z(s)$, the image of the interface $y = 2\alpha - \eta(x)$ with respect to the upper surface of the upper layer $y = \alpha$, an infinitely small semi-circle bypassing its center $z(s)$ in the upper layer, and two vertical lines $x = \pm L$ connecting the interface and its

image as $L \to +\infty$. By virtue of the asymptotic properties of $G_1(z)$:

$$G_1(z) \to 0,\ x \to -\infty$$

and

$$\|G_1\| < +\infty,\ \|G_1(z)\| = o(|z|),\quad x \to +\infty,$$

one can know that the contributions from $x = \pm L$ are both zero. Considering the unpenetrable condition (2.4), the imaginary part of (2.6) gives

$$\begin{aligned}\pi(c - x'(s)\phi_1'(s)) = &\int_{-\infty}^{+\infty} \frac{\begin{vmatrix} x(t)-x(s) & y(t)-y(s) \\ cx'(t)-\phi_1'(t) & cy'(t) \end{vmatrix}}{(x(t)-x(s))^2+(y(t)-y(s))^2}\,\mathrm{d}t+\\ &\int_{-\infty}^{+\infty} \frac{\begin{vmatrix} x(t)-x(s) & y(t)+y(s)-2\alpha \\ cx'(t)-\phi_1'(t) & cy'(t) \end{vmatrix}}{(x(t)-x(s))^2+(y(t)+y(s)-2\alpha)^2}\,\mathrm{d}t. \end{aligned} \tag{2.9}$$

One can see [12, 16] for more details. In addition, comparing with the full form as in [12, 16, Eq. (15)]

$$\begin{aligned}\pi(c - x'(s)\phi_1'(s)) = &\int_{-\infty}^{+\infty} \frac{(\phi_1'(t)-cx'(t))(y(t)-y(s))+cy'(t)(x(t)-x(s))}{(x(t)-x(s))^2+(y(t)-y(s))^2}\,\mathrm{d}t+\\ &\int_{-\infty}^{+\infty} \frac{(\phi_1'(t)-cx'(t))(y(t)+y(s)-2\alpha)+cy'(t)(x(t)-x(s))}{(x(t)-x(s))^2+(y(t)+y(s)-2\alpha)^2}\,\mathrm{d}t,\end{aligned}$$

we use the matrix form in (2.9) to make it more compact.

Similarly, for the lower layer, an analytical function

$$G_2(z) = \frac{\mathrm{d}f_2}{\mathrm{d}z} - 1$$

is introduced. Since $z = z^*$, the location of the doublet, is an isolated singularity of G_2, we turn to apply the residue theorem to establish the corresponding boundary integral equation

$$\oint_{\Gamma_2} \frac{G_2(\xi)}{\xi - z}\,\mathrm{d}\xi - \pi\mathrm{i}G_2(z) = 2\pi\mathrm{i}\mathrm{Res}\{\frac{G_2(\xi)}{\xi - z}, z^*\}. \tag{2.10}$$

The integral path Γ_2 consists of the interface excluding the fixed point $z = z(s)$, an infinite small semi-circle centering $z = z(s)$ and bypassing this point in the lower layer, and a semicircle submerged in the lower layer with a large radius R as $R \to +\infty$. Concerning (2.2), $z^* = -\mathrm{i}$ is a second-order pole of $G_2(\xi)$. The residual at z^* is obtained as follows:

$$\mathrm{Res}\{\frac{G_2(\xi)}{\xi - z}, z^*\} = \lim_{\xi \to z^*} \frac{\mathrm{d}}{\mathrm{d}\xi}[(\xi - z^*)^2 \frac{G_2(\xi)}{\xi - z}] = \frac{m}{2\pi(z(s) + \mathrm{i})^2}. \tag{2.11}$$

Inserting it into (2.10), and taking the imaginary part of (2.10) gives

$$\begin{aligned}\pi(x'(s)\phi_2'(s) - 1) = &\int_{-\infty}^{+\infty} \frac{\begin{vmatrix} x(t)-x(s) & y(t)-y(s) \\ x'(t)-\phi_2'(t) & y'(t) \end{vmatrix}}{(x(t)-x(s))^2+(y(t)-y(s))^2}\,\mathrm{d}t+\\ &\frac{m((y(s)+1)^2 - x^2(s))}{(x^2(s)+(y(s)+1)^2)^2}.\end{aligned} \tag{2.12}$$

At this time the governing Eqs. (2.6), (2.7), (2.9), and (2.12) with the radiation conditions (2.3) are all derived. $x(s)$, $y(s)$, $\phi_1(s)$, $\phi_2(s)$ can be calculated by numerical methods.

3. Linear solutions

An approximate solution may be derived when the dimensionless strength of the doublet is small; that is to say, $|m| \ll 1$. Firstly we express the interface and the velocity potentials as follows:

$$\phi_1(x,y) = cx + m\phi_1^{(1)}(x,y) + O(m^2), \quad \phi_2(x,y) = x + m\phi_2^{(1)}(x,y) + O(m^2),$$
$$\eta(x) = m\eta^{(1)}(x) + O(m^2). \tag{3.1}$$

The linearized kinematic conditions and the linearized Bernoulli's equation are

$$\frac{\partial \phi_1^{(1)}}{\partial y} = c\frac{\mathrm{d}\eta^{(1)}}{\mathrm{d}x}, \ \frac{\partial \phi_2^{(1)}}{\partial y} = \frac{\mathrm{d}\eta^{(1)}}{\mathrm{d}x}, \quad y = 0 \tag{3.2}$$

and

$$\rho c\frac{\partial \phi_1^{(1)}}{\partial x} - \frac{\partial \phi_2^{(1)}}{\partial x} + \frac{\rho - 1}{F^2}\eta^{(1)} = 0 \tag{3.3}$$

on the interface, respectively. The kinetic conditions of surface of the upper layer is sitll (2.4). In the following we briefly describe the process of solving this linearised problem.

Assuming the velocity potential are in the form [12]

$$\phi_1^{(1)} = \frac{1}{2\pi}\int_0^{+\infty} [B(k)\mathrm{e}^{-ky} + C(k)\mathrm{e}^{ky}]\mathrm{e}^{\mathrm{i}k(x-x_0)}\,\mathrm{d}k, \tag{3.4}$$

$$\phi_2^{(1)} = \frac{1}{2\pi}(\frac{1}{z - z_0} + \frac{1}{z - \overline{z_0}}) + \frac{1}{2\pi}\int_0^{+\infty} A(k)\mathrm{e}^{k(y-h)+\mathrm{i}k(x-x_0)}\,\mathrm{d}k \tag{3.5}$$

due to a doublet located at $(x_0, -h)$, $h > 0$, where $z_0 = x_0 - \mathrm{i}h$, and $\overline{z_0}$ is the complex conjugate of z_0. Here z_0 represents the location of the singularity. The symbol "Re[·]" on the right hands of both (3.4) and (3.5) are neglected. Inserting them into the linearised boundary conditions (2.4) and (3.2), we have

$$C(k) = B(k)e^{-2k\alpha}, \quad B(k) = -\frac{cA(k)e^{k(\alpha-h)}}{2\sinh(k\alpha)}. \tag{3.6}$$

To solve $A(k)$, the first term of the right hand of (3.5) is transformed into the formulation of an integral via the following expression:

$$\frac{x^2 - y^2}{(x^2 + y^2)^2} = \mathrm{Re}\Big[\int_0^{+\infty} k\mathrm{e}^{-kx+\mathrm{i}ky}\mathrm{d}k\Big], \quad x > 0, \tag{3.7}$$

This formulation is obtained from the fact that the Laplace transformation of k is

$$\int_0^{\infty} k\mathrm{e}^{-sk}\mathrm{d}k = 1/s^2.$$

Replacing s by $x - \mathrm{i}y$ of both sides and then its real part gives (3.7). Now taking the derivative of both sides of (3.3) with respect to x and using (3.2), (3.4), (3.5), (3.6) associated with (3.7),

one obtain

$$A(k) = \frac{2\mathrm{i}F^2 k \sinh(k\alpha)}{Q(k)}, \tag{3.8}$$

where

$$Q(k) = (F^2 k + \rho - 1)\sinh(k\alpha) + \rho c^2 F^2 k \cosh(k\alpha). \tag{3.9}$$

The expression of $\eta^{(1)}$ is obtained from the linearised Bernoulli's Eq. (3.3):

$$\eta^{(1)} = \frac{F^2}{\pi(1-\rho)}\Big\{\int_0^{+\infty} \frac{P(k)}{Q(k)} \mathrm{e}^{-kh+\mathrm{i}k(x-x_0)}\,\mathrm{d}k + \frac{(x-x_0)^2 - h^2}{((x-x_0)^2+h^2)^2}\Big\}, \tag{3.10}$$

where

$$P(k) = F^2 k^2(\rho c^2 \cosh(k\alpha) + \sinh(k\alpha)).$$

The property of $Q(k)$ is important in evaluating the integral in (3.10). In the following we briefly discuss when $Q(k)$ has one positive roots. In other words, when is the integral in (3.10) a singular one?

At first, it is easy to show that

$$Q(k) \sim \frac{F^2(\rho c^2+1)}{2} k e^{k\alpha},\ Q'(k) \sim \frac{\alpha F^2(\rho c^2+1)F^2 k}{2} k e^{k\alpha},\quad k \to +\infty.$$

Thus $Q(k), Q'(k) > 0$ when k is sufficient large. Next examine the property of $Q(k)$ near $k = 0$:

$$Q(k) \sim (\rho c^2 F^2 + \alpha(\rho - 1))k = Q'(0)k,\quad k \to 0$$

and

$$Q(0) = 0,\ Q'(0) = \rho c^2 F^2 + \alpha(\rho - 1),\ Q''(0) = 2F^2\alpha > 0.$$

One can easily verify that $Q'(k) > 0$ when $Q'(0) \geq 0$, so $Q(k) > 0$ for $k > 0$. On the other hand, if $Q'(0) < 0$, then $Q(k) < 0$ in the neighborhood of $k = 0$. According to the intermediate value theorem of continuous functions, there exists one positive root of $Q(k)$, which is denoted as k_0. In practice, it is also the unique positive root.

Now the existence/nonexistence of k_0 determines the evaluation of the integral in (3.10):

(1) If $Q'(0) \geq 0$, the integral in (3.10) is just an ordinary integral. Replacing x_0, h by 0, 1, respectively, then from (3.1) and (3.10) we have

$$\eta = \frac{mF^2}{\pi(1-\rho)}\Big\{\int_0^{+\infty} \frac{P(k)}{Q(k)} \mathrm{e}^{-k}\cos(kx)\,\mathrm{d}k + \frac{x^2-1}{(x^2+1)^2}\Big\} + O(m^2). \tag{3.11}$$

Moreover, based on the stationary phase method [18], $\eta \sim 0$ as $x \to +\infty$. That is to say, in this case there is only local elevation of the interface near the submerged doublet.

(2) If $Q'(0) < 0$, the integral in (3.10) is a singular integral and is evaluated in the meaning of Cauchy principal values. Here only the result is listed:

$$\eta(x) = \frac{mF^2}{\pi(1-\rho)}\Big\{\int_0^{+\infty} R(k)\mathrm{e}^{-k}\cos(kx)\,\mathrm{d}k - \frac{2\pi P(k_0)}{Q'(k_0)}\mathrm{e}^{-k_0}H(x)\sin k_0 x + R_1 + R_2\Big\} + O(m^2), \tag{3.12}$$

where

$$R(k) = \frac{P(k)}{Q(k)} - \frac{P(k_0)}{Q'(k_0)(k-k_0)},\ R_1 = \frac{P(k_0)}{Q'(k_0)}\mathrm{Re}[\mathrm{e}^{-k_0+\mathrm{i}k_0 x}E_1(-k_0+\mathrm{i}k_0 x)],\ R_2 = \frac{x^2-1}{(x^2+1)^2}.$$

H$(\cdot)$ means the Heaviside step function, and $E_1(\cdot)$ denotes the complex exponential integral function:

$$E_1(z) = \int_z^\infty \frac{\mathrm{e}^{-t}}{t}\mathrm{d}t = \int_1^\infty \frac{\mathrm{e}^{-zt}}{t}\mathrm{d}t.$$

Again, based on the stationary phase method [18], following asymptotic behavior of the linear solution (3.12) for large x

$$\eta \sim \frac{2mF^2P(k_0)}{(\rho-1)Q'(k_0)}\mathrm{e}^{-k_0}\sin k_0 x, \quad x \to +\infty, \tag{3.13}$$

is obtained. The wavenumber k_0 is the positive root of $Q(k)$. And the steady downstream wave height of the linear solutions is

$$h = \frac{4mF^2P(k_0)}{(1-\rho)Q'(k_0)}\mathrm{e}^{-k_0}. \tag{3.14}$$

Remark 3.1 Since $Q(k_0) = 0$ one has

$$\tanh(k_0\alpha) = \frac{\rho c^2F^2k_0}{1-\rho-F^2k_0}. \tag{3.15}$$

Based on the fact that $\tanh(k_0\alpha) < 1$, we obtain the following bounds of the wavenumber k_0:

$$0 < k_0 < \frac{1-\rho}{F^2(1+\rho c^2)}. \tag{3.16}$$

Thus $k_0 \to 0$ as $F \to +\infty$ or $\rho \to 1$, which means that steady wave length becomes infinite and in fact there are not any downstream waves. In fact, the expression (3.12) will be replaced by (3.11) as if $F^2 \geq \alpha(1-\rho)/\rho c^2$ or $\rho \geq \alpha/(c^2F^2+\alpha)$, since the condition $Q'(0) = \rho c^2F^2 + \alpha(\rho-1) < 0$ must be satisfied.

Remark 3.2 Moreover, if we set $K_0 := \frac{1-\rho}{F^2(1+\rho c^2)}$, then a simple result $k_0 = K_0$ may be obtained for sufficiently large α, which comes from the fact that making $\alpha \to +\infty$ in (3.15) leads to the result $k_0 \to K_0$.

4. Numerical methods for the nonlinear solutions

In this section, we present the numerical method to obtain the fully nonlinear solutions to the problem. The numerical procedures applied here are similar to that in [12,15–17]. Governing Eqs. (2.6), (2.7), (2.9), and (2.12) with the radiation conditions (2.3) will be discretized to get the nonlinear equations, and then a classical quasi-Newton method [19] is applied to solve this system of equations. At first, the infinite integral interval $(-\infty, +\infty)$ is truncated to a finite interval (E_-, E_+) and N grids

$$s_k = E_- + (k-1)\Delta s, \quad k = 1, 2, \ldots, N$$

are obtained, where

$$\Delta s = (E_+ - E_-)/(N-1).$$

x_k, y_k, x'_k, y'_k, $\phi_{1,k}$, $\phi_{2,k}$, $\phi'_{1,k}$, $\phi'_{2,k}$ are the approximate values of undetermined variables $x(s)$, $y(s)$, $x'(s)$, $y'(s)$, $\phi_1(s)$, $\phi_2(s)$, $\phi'_1(s)$, $\phi'_2(s)$ at $s = s_k$. If the approximate values of y'_k are

determined, x'_k are calculated from the arclength condition (2.6), and then x_k, y_k may be obtained by the trapezoidal rule. Here $x_1 = E_-$, $y_1 = 0$, $x'_k = 1$, $y'_k = 0$ are determined from the radiation conditions (2.3) and the arclength condition (2.6). Next, using the composite trapezoidal rule on the integral Eq. (2.9) leads to a system of equations in the matrix form

$$\mathbf{A}\mathbf{\Phi}'_1 = \mathbf{b}, \tag{4.1}$$

where

$$\mathbf{\Phi}'_1 = (\phi'_{1,2}, \ldots, \phi'_{1,N})^{\mathrm{T}}.$$

Solving (4.1), we may obtain $\phi'_{1,k}$, $k = 2, \ldots, N$.

Remark 4.1 In practice, if the strength m is too large or the step length Δs is too small, solving it directly may cause disastrous results in the whole numerical calculations. This problem comes from the fact that (4.1) may become an ill-posed system due to the compactness of the integral operator in (2.9). Based on the well-known Tikhonov regularization method in inverse problem theory [20], a normal equation

$$(\mathbf{A}^{\mathrm{T}}\mathbf{A} + \theta\mathbf{I})\mathbf{\Phi}'_1 = \mathbf{A}^{\mathrm{T}}\mathbf{b} \tag{4.2}$$

instead of (4.1) is calculated to recover the well-posedness, where $\mathbf{I}$ is the identity matrix and θ is the regularization parameter. In numerical experiments, we fix θ with a small value (e.g. $\theta = 2 \times 10^{-3}$) and adjust it based on the performance of the regularization method until this remedy moves away the effects of the ill-posedness. We also verify the consistency of numerical results with and without the regularization when the system is not ill-posed.

From Bernoulli's Eq. (2.7), values of $\phi'_{2,k}$ are easily obtained. The remaining Eq. (2.12) is chosen as the cost function. Again using the composite trapezoidal rule, the discrete version of (2.12) is formulated as

$$\mathbf{E}(\mathbf{u}) = \mathbf{0}, \tag{4.3}$$

where

$$\mathbf{E} = (E_2(\mathbf{u}), \ldots, E_N(\mathbf{u}))^{\mathrm{T}}, \ \mathbf{u} = (\mathbf{y'_2}, \ldots, \mathbf{y'_N})^{\mathrm{T}}.$$

Broyden's rank-1 method [19], one kind of quasi-Newton method, is applied to solve this nonlinear system until $\|\mathbf{u}\| < \sigma$:

$$\begin{cases} \mathbf{u}^{(i+1)} = \mathbf{u}^{(i)} - (\mathbf{B}^{(i)})^{-1}\mathbf{E}(\mathbf{u}^{(i)}) \\ \mathbf{B}^{(i+1)} = \mathbf{B}^{(i)} + \left(\mathbf{f}_i - \mathbf{B}^{(i)}\mathbf{s}_i\right)\mathbf{s}_i^{\mathrm{T}} / \left(\mathbf{s}_i^{\mathrm{T}}\mathbf{s}_i\right) \end{cases}, \quad i = 0, 1, 2, \ldots \tag{4.4}$$

where

$$\mathbf{s}_i = \mathbf{u}^{(i+1)} - \mathbf{u}^{(i)}, \ \mathbf{f}_i = \mathbf{E}(\mathbf{u}^{(i+1)}) - \mathbf{E}(\mathbf{u}^{(i)}).$$

$\mathbf{B}^{(i)}$ and $\mathbf{u}^{(i)}$ are the approximate value of $\mathbf{u}$ and the approximate Jacobian matrix in the i-th iteration. In the whole paper, the initial guess of $\mathbf{u} = (y'_k)$, $k = 2, \ldots, N$, is set to be zero. And the initial approximate Jacobian matrix $\mathbf{B}^{(0)}$ is calculated via the forwarding difference at the initial guess of y'_k:

$$\mathbf{B}^{(0)} = ((\mathbf{E}(h\mathbf{e}_1) - \mathbf{E}(\mathbf{0}))/h, \ldots, (\mathbf{E}(h\mathbf{e}_{N-1}) - \mathbf{E}(\mathbf{0}))/h)_{(N-1)\times(N-1)}, \tag{4.5}$$

where $\mathbf{e}_j$ is the j-th unit vector in $N-1$ dimension Euclidean space, $j = 1, \ldots, N-1$.

5. Results analysis

In this section, we present the results of linear and nonlinear internal wave profiles, including the effects of the sign of doublet and its strength on the wave profiles, comparisons between the wave profiles due to a doublet and that due to a point vortex [12]. Here are some detailed parameters used in the following text. The calculating domain is set to be $(E_-, E_+) = (-20, 20)$, the grid number $N = 2001$, and the step length is $\Delta s = 0.02$. The depth of the upper layer is $\alpha = 20$. The far upstream uniform velocity $c = 1$, and the density ratio $\rho = 0.9$. The Froude number is fixed to be $F = 0.1$ unless it is necessary.

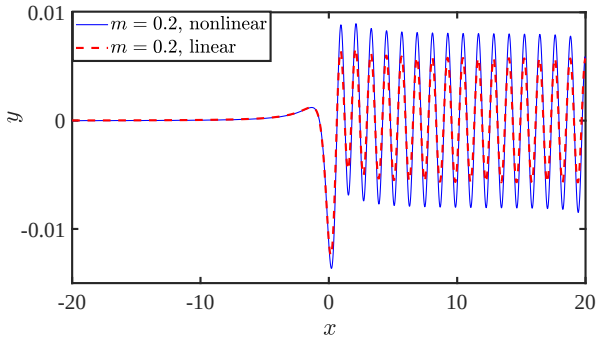

Figure 2 Comparisons between nonlinear and linear solutions due to a doublet

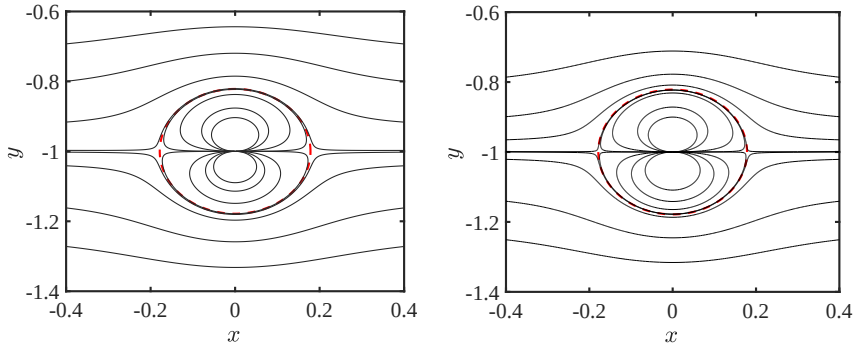

(a) Streamlines for nonlinear solutions (b) Streamlines for linear solutions

Figure 3 Comparisons of streamlines between (a) nonlinear and (b) linear solutions

5.1. Wave profiles

Figure 2 compares the wave profiles between nonlinear (blue solid) and linear (red dashed) solutions. One can see that wave profiles for nonlinear and linear solutions are quite similar. One of the difference between nonlinear and linear solutions is the amplitudes of downstream waves. Besides, the locations of crests and troughs are slightly different after carefully examining wave profiles of both nonlinear and linear solutions. Moreover, streamline contours, $\psi_2(x, y) = \text{const}$,

of both nonlinear and linear solutions are examined in Figure 3. The circle (red dashed line) in Figure 3 represent a cylinder of radius $\sqrt{m/2\pi}$ located at the original point. Two points should be noticed. The first one is that there are not any closed streamlines, like [13] emphasized. The second one is that the topologies of streamlines of both solutions are quite similar globally. Differences of locations of streamlines come from the fact that different constant numbers are chosen in $\psi_2(x, y) = \text{const}$. In fact, nonlinear boundary conditions along the interface seldom influences the topology structures of streamlines fields near the submerged singularity.

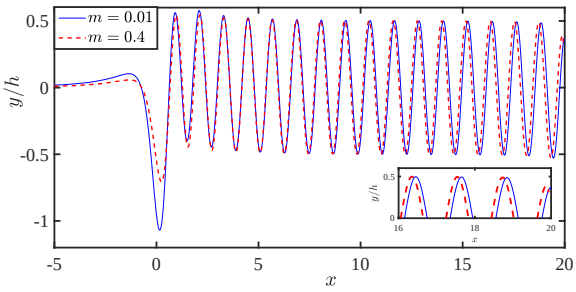

(a) (Scaled) wave profiles of nonlinear results

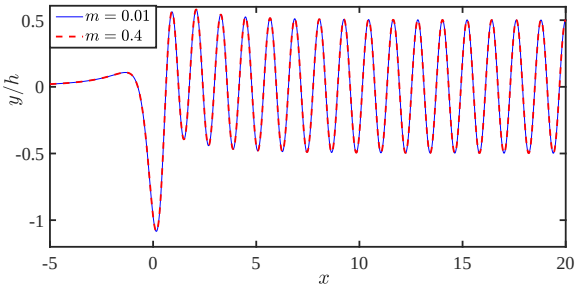

(b) (Scaled) wave profiles of linearized results

Figure 4 Comparisons of scaled wave profiles y/h between (a) nonlinear and (b) linear results for different strength of the doublet

To further examine the nonlinear effects, wave profiles for different strength of the doublet are checked. Figure 4 shows the scaled wave profiles $y(x)/h$ of both nonlinear and linear results, where h is the corresponding downstream wave height. Here the scaling factor $1/h$ is used to eliminate the effects of increasing strength on the wave heights. Furthermore, according to Eqs. (3.1), (3.10) and (3.14), the scaled wave profiles of linearized solutions is only

$$y = \frac{(1-\rho)Q'(k_0)}{4F^2P(k_0)}\mathrm{e}^{k_0}\eta^{(1)}(x),$$

which is independent of m. Thus the scaled wave profiles of linear results are invariant with m, as Figure 4 (b) shows. On the other hand, Figure 4 (a) demonstrates the significant difference of nonlinear wave profiles for different strengths of the doublet, especially for the first wave. Besides, the wave profiles move upstream a bit when m increases. These two points are not true for linear results.

5.2. Effects of the strength and the Froude number

However, this wave-less solution may not be supported by nonlinear results. Figure 6 compares the wave profiles of both nonlinear (blue solid) and linear (red dashed) solutions for the large Froude number. Here the Froude number is set to be $F = 2$, and the strength of the doublet is $m = 0.5$. In particular, the elevation of nonlinear wave profiles near $x = 60$ seems to be part of waves with a large wave length. However, this elevation is only about 10^{-3}, and this may come from the numerical errors. More efficient numerical procedures which can evaluate large domains need to be explored in the future to examine this problem.

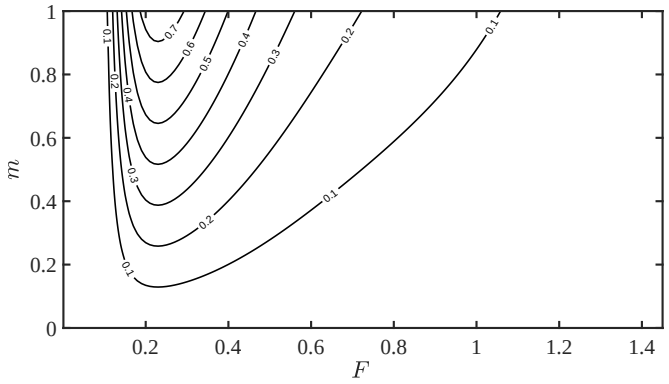

Figure 5 Contour of wave heights for the strength of the doublet and the Froude number

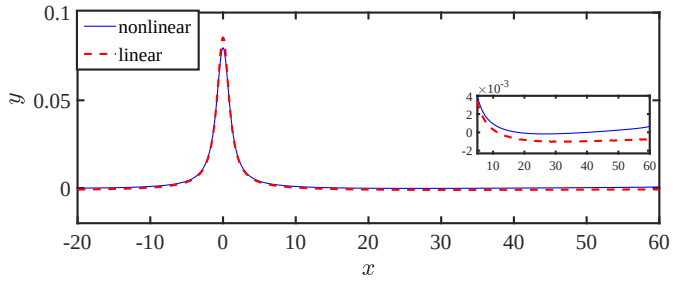

Figure 6 Comparisons of wave profiles between nonlinear and linear results for large Froude number

Figure 5 shows the relationship between the steady downstream wave height h and the parameter pair (F, m). Here only the linear results are shown, since both nonlinear and linear results have the same global characteristics. One can see the ridge near $F = 0.22$, where wave heights are quite larger than in other cases. When $F \leq 0.2$, contour lines are much dense, thus wave heights may fast increase when F increases and F is small. If F is large, contour lines become sparse, and wave heights decrease slowly as F increases. In fact, based on the analysis in Section 5.3, when $F \geq \sqrt{\alpha(1-\rho)/\rho c^2}$, the expression of linear interfacial waves becomes (3.11) instead of (3.12). Thus the steady downstream wave profiles disappear in linear solutions. Besides, if the Froude number of the upper layer is used:

$$F_1 = c_1/\sqrt{gT} = (c/\sqrt{\alpha})F,$$

then one can obtain the critical Froude number of the upper layer:

$$(c/\sqrt{\alpha})\sqrt{\alpha(1-\rho)/\rho c^2} = \sqrt{1/\rho - 1}.$$

That is to say, the critical upper-layer Froude number only depends on the density ratio.

5.3. Comparisons between wave profiles due to one doublet and one vortex

A point vortex can be seen as the limit of a moving object. To compare the results of different types of singularities, firstly we examine the expressions of nonlinear and linear solutions. Comparing nonlinear boundary integral equations for both a point vortex in [12] and a doublet in this work, the only difference is that the first term of the right hand in [12, Eq. (20)] is replaced by

$$\frac{m((y(s)+1)^2 - x^2(s))}{(x^2(s)+(y(s)+1)^2)^2}$$

in (2.12). Besides, difference between both linear solutions is that the term $-1/(x^2+1)$ is replaced by $(x^2-1)/(x^2+1)^2$ in (2.12). Primary properties of these interfacial waves may be determined by the configurations of the two-layer systems instead of the involved singularities. Here we present comparisons between the results due to one doublet and one point vortex.

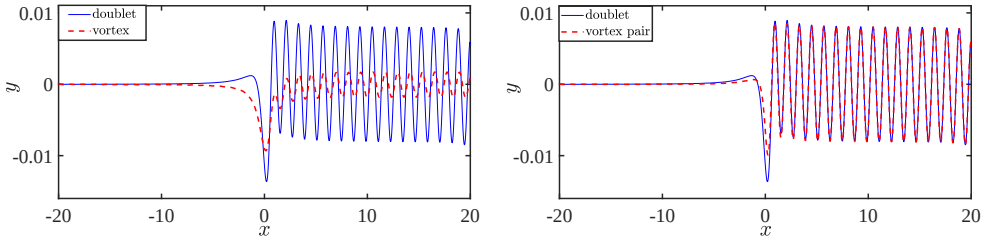

(a) Wave profiles due to a doublet and a vortex

(b) Wave profiles due to a doublet and a vertical vortex pair

Figure 7 Comparisons of wave profiles due to a doublet and a point vortex/a vertical vortex pair

Figure 7 (a) presents the nonlinear wave profiles for one doublet and one point vortex of strength $\epsilon > 0$. Here both strengths of two types of singularities are set to be equal, i.e., $m = \epsilon = 0.2$. One can see the significant difference between downstream wave heights due to a doublet and those due to a point vortex. In fact, the former is about 4.56 times the latter. Besides, a small bump occurs at the upstream location of the first large trough. This bump, which may come from the three term $(x^2-1)/(x^2+1)^2$ in the right hand of (3.12), can also be found in the case of interfacial waves due to a hydrofoil [17], while it does not appear in the case of one point vortex. This may be a characteristic of interfacial waves due to a submerged body at a small Froude number, e.g., $F = 0.1$.

Moreover, recalling the fact that a doublet can be seen as the limit of a vertical equal-strength counter-rotating vortex pair as the distance tends to zero, next we examine the wave profiles with a vortex pair of strength $\epsilon = \pm m/2$ located at $(0, -1 \pm d)$. Figure 7 (b) shows that when d is

set to be 0.49 and $m = 0.2$, downstream wave profiles due to a doublet are quite consistent with those due to a vertical vortex pair. The differences are mainly the amplitudes of the first trough and the bump at the upstream location of the first trough. This may not be surprise, since the vertical vortex pair in the uniform flows leads to the Kelvin oval. In particular, it is worth noting that if other parameters change and d is still 0.49, then this consistency will be broken. For the sake of simplicity, a quantity d_c is used. If the distance between the vertical vortex pair of strength $\pm m/2$ is set to be $d = d_c$, then the downstream waves due to this vortex pair is consistent with those due to a doublet of strength m.

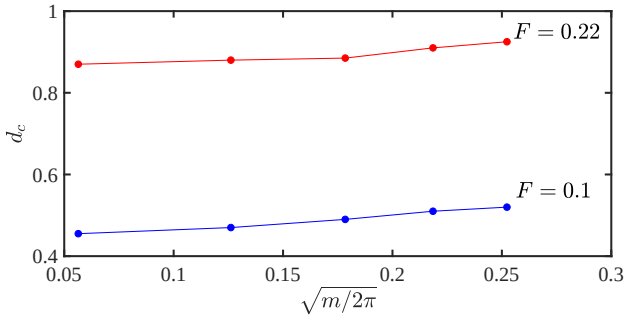

Figure 8 Relationships between d_c and $\sqrt{m/2\pi}$

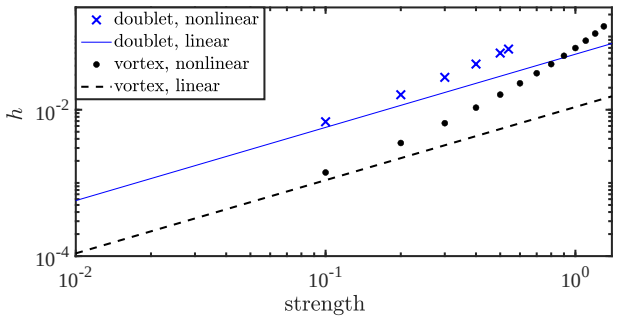

Figure 9 Comparisons of wave heights h due to point vortex and doublet of different strength

To further examine this consistency, here we check the relationship between d_c and m. Figure 8 describes how the critical value d_c changes with $\sqrt{m/2\pi}$ increasing. One can notice the big difference for different values of Froude number. This can be explained as follows. First, recalling results in [21] that constructive/destructive interference occurs for the case of vortex pair. This interference is related to the downstream wave length. If the wave length is large, then the distance between the vortex pair should be adjusted to be larger to maintain the effect of the interference. Next, from the analysis in Remark 3.1 of Section 3, the downstream wave length becomes larger if the Froude number F increases. As a result, the distance between the vortex pair must become larger to main the consistency when F becomes larger. Besides, one can observe that d_c increases slightly if m becomes large. This is not true for linearized results, since the downstream wave length does not change with the strength of the singularity.

Considering the large difference in downstream wave heights of these two singularities, now we examine the effects of changing strengths of the doublet/point vortex on the downstream wave height, as shown in Figure 9. Significant differences between nonlinear and linear results with both singularities reflect the strong influences of nonlinearity. Besides, nonlinear wave heights due to a vortex are about $O(\epsilon^3)$ and those due to a doublet are only $O(m^2)$, though the former is quite smaller than the latter. In fact, from the linear results one can see that wave height due to a doublet is k_0 times those due to a vortex, where k_0 is the wave number. This can be also found in Figure 9, where the slope of line representing the linear results of a doublet is about 5.26 times that of a vortex and $k_0 = 5.26$ under the parameter used here. Totally, the influence of the nonlinearity of a doublet is slightly smaller than that of a point vortex.

6. Conclusions

In this paper, the nonlinear solution and linear analytical solution of the interface internal wave when the doublet is located in the infinitely deep lower layer of fluids are calculated. The difference between the linear solution and the nonlinear solution is analyzed, and comparisons between the interfacial wave caused by the point vortex and that due to the doublet are presented. Though wave profiles of nonlinear and linear solutions are quite similar, the significant differnce of downstream wave heights are observed. Besides, with the strength of the doublet increases, the nonlinearity is reflected on the fact that the amplitude of the first wave becomes smaller, and the downstream wave profiles slightly move toward the upstream direction. Therefore, high-order corrections upon linear solutions may be important, which should be examined in future works. The first crest is quite smaller than the following waves such that one can identify it as a small bump at the upstream location of the wave train. This may also be a characteristic of the interfacial waves due to a submerged body. Froude number have important influence on the downstream wave height. Wave height quickly goes to the extreme point, which is not too large, as the Froude number increases. Downstream wave profiles may disappear for a large Froude number, and then wave-less solutions are obtained. Finally, wave heights with a doublet are about k_0 times those with a point vortex, where k_0 is the wave number. Besides, When a vertical equal-strength counter-rotating pair is used to compare it with the case of a doublet, it is found that the wave profiles can be quite close if the distance between the vortex pair is set to be certain values.

Acknowledgements We thank the referees for their time and comments.

References

[1] Xiaodong HUANG, Zhaohui CHEN, Wei ZHAO, et al. *An extreme internal solitary wave event observed in the northern South China Sea*. Scientific Reports, 2016, **6**(1): 30041.

[2] Pengxu ZOU, J. D. BRICKER, W. S. J. UIJTTEWAAL. *The impacts of internal solitary waves on a submerged floating tunnel*. Ocean Engineering, 2021, **238**: 109762.

[3] Min CHEN, Ke CHEN, Yunxiang YOU, et al. *Experimental study of forces on a multi-column floating platform in internal solitary waves*. Appl. Ocean Res., 2018, **78**: 192–200.

[4] C. R. JACKSON, J. B. DA SILVA, G. JEANS. *The generation of nonlinear internal waves*. Oceanography, 2012, **25**(2): 108–123.

[5] M. H. ALFORD, T. PEACOCK, J. A. MACKINNON, et al.. *The formation and fate of internal waves in the South China Sea*. Nature, 2015, **521**(7550): 65–69.

[6] Zhan WANG, Yuke ZHU. *Theory, modelling and computation of nonlinear ocean internal waves*. Chinese J. Mech. (Bejing), 2019, **51**(6): 1589–1604.

[7] J. V. WEHAUSEN, E. V. LAITONE. *Surface Waves*. Springer Berlin Heidelberg, Berlin, 1960.

[8] N. E. KOCHIN, I. A. KIBEL, N. V. ROZE. *Theoretical Hydromechanics*. Wiley Interscience, New York, 1964.

[9] M. A. GORGUI, S. E. KASSEM. *Basic singularities in the theory of internal waves*. Quart. J. Mech. Appl. Math., 1978, **31**(1): 31–48.

[10] R. W. YEUNG, T. C. NGUYEN. *Waves generated by a moving source in a two-layer ocean of finite depth*. J. Engrg. Math., 1999, **35**(1-2): 85–107.

[11] Gang WEI, Dongqiang LU, Shiqiang DAI. *Waves induced by a submerged moving dipole in a two-layer fluid of finite depth*. Acta Mech. Sin., 2005, **21**(1): 24–31.

[12] Zhen WANG, Li ZOU, Hui LIANG, et al. *Nonlinear steady two-layer interfacial flow about a submerged point vortex*. J. Engrg. Math., 2017, **103**(1): 39–53.

[13] R. PETHIYAGODA, S. W. MCCUE, T. J. MORONEY. *What is the apparent angle of a Kelvin ship wave pattern?* J. Fluid Mech., 2014, **758**: 468–485.

[14] R. PETHIYAGODA, T. J. MORONEY, C. J. LUSTRI, et al. *Kelvin wake pattern at small Froude numbers*. J. Fluid Mech., 2021, **915**: Paper No. A126, 28 pp.

[15] L. K. FORBES. *On the effects of non-linearity in free-surface flow about a submerged point vortex*. J. Engrg. Math. 1985, **19**(2): 139–155.

[16] S. R. BELWARD, L. K. FORBES. *Fully non-linear two-layer flow over arbitrary topography*. J. Engrg. Math., 1993, **27**(4): 419–432.

[17] Zhen WANG, Changhong WU, Li ZOU, et al. *Nonlinear internal wave at the interface of two-layer liquid due to a moving hydrofoil*. Phys. Fluids, 2017, **29**(7): 072107.

[18] C. M. BENDER, S. A. ORSZAG. *Advanced Mathematical Methods for Scientists and Engineers I: Asymptotic Methods and Perturbation Theory*. Springer, New York, 1999.

[19] J. E. DENNIS JR, J. J. MORE. *Quasi-Newton methods, motivation and theory*. SIAM Rev., 1977, **19**(1): 46–89.

[20] A. KIRSCH. *An Introduction to the Mathematical Theory of Inverse Problems*. Springer, New York, 2011.

[21] Zhen WANG, Di LIU, Xiaoqin AN. *Interference of internal waves due to two point vortices: linear analytical solution and nonlinearinteraction*. R. Soc. Open Sci., 2022, **9**: 211476.